



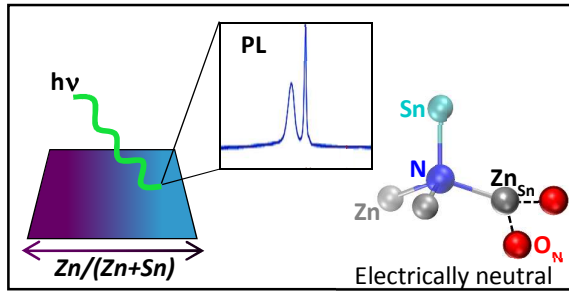
Exciton Photoluminescence and Benign Defect Complex Formation in Zinc Tin Nitride

Journal:	<i>Materials Horizons</i>
Manuscript ID	MH-COM-04-2018-000415.R1
Article Type:	Communication
Date Submitted by the Author:	12-Jun-2018
Complete List of Authors:	<p>Fioretti, Angela; National Renewable Energy Lab; Colorado School of Mines Pan, Jie; National Renewable Energy Laboratory Ortiz, Brenden; Colorado School of Mines Melamed, Celeste; National Renewable Energy Laboratory, ; Colorado School of Mines Dippo, Patricia; National Renewable Energy Laboratory, Schelhas, Laura; SLAC National Accelerator Laboratory Perkins, John; National Renewable Energy Laboratory, Kuciauskas, Darius; National Renewable Energy Laboratory Lany, Stephan; National Renewable Energy Laboratory Zakutayev, Andriy; National Renewable Energy Laboratory Toberer, Eric; National Renewable Energy Laboratory; Colorado School of Mines Tamboli, Adele; National Renewable Energy Lab; Colorado School of Mines, Physics</p>

*Conceptual Insights**Exciton Photoluminescence and Benign Defect Complex Formation in Zinc Tin Nitride*

Ternary and multinary semiconductors provide chemical flexibility for tuning material properties such as doping and bandgap, but often suffer from atomic disorder detrimental to electrical transport. This tradeoff has led to a paradigm in which researchers assume ordered, defect-free material is prerequisite to device-grade electronic quality. This backdrop motivated our investigation into the structural and electronic properties of off-stoichiometric zinc tin nitride (ZTN), in which zinc-rich composition suppresses degenerate carrier concentration but leads to significant point defect density and raises concerns about nonradiative recombination. The main conceptual insight of this work is that benign defect complex formation can be a general mechanism underpinning defect tolerance in disordered materials. The critical finding is that by intentionally forming $\text{Zn}_{\text{Sn}}\text{-}2\text{O}_{\text{N}}$ neutral defect complexes, a material with an extremely high defect density and can be induced to emit excitonic photoluminescence – a key descriptor of excellent material functionality for optoelectronic applications. The implications of this finding extend well beyond researchers interested in ZnSnN_2 , as inducing “defect tolerance” is the key to enabling new and low-cost materials to find viable applications, for example in solar energy. As such, this paper presents a new design principle for materials discovery and development.

Table of Contents Entry

Exciton Photoluminescence and Benign Defect Complex Formation in Zinc Tin Nitride

Exciton photoluminescence is observed in disordered zinc tin nitride as a result of benign defect complex formation encouraged by annealing.

Exciton Photoluminescence and Benign Defect Complex Formation in Zinc Tin Nitride

Angela N. Fioretti,^{1,2} Jie Pan,¹ Brenden R. Ortiz,² Celeste L. Melamed,^{1,2}
Patricia C. Dippo,¹ Laura T. Schelhas,³ John D. Perkins,¹ Darius Kuciauskas,¹
Stephan Lany,¹ Andriy Zakutayev,¹ Eric S. Toberer,^{1,2}
and Adele C. Tamboli^{1,2*}

¹National Renewable Energy Laboratory, Golden, Colorado 80401 USA

²Colorado School of Mines, Golden, Colorado 80401 USA

³Applied Energy Programs, SLAC National Accelerator Laboratory, Menlo Park, California 94025 USA

*To whom correspondence should be addressed

E-mail: adele.tamboli@nrel.gov

Abstract

Emerging photovoltaic materials need to prove their viability by demonstrating excellent electronic properties. In ternary and multinary semiconductors, disorder and off-stoichiometry often cause defects that limit the potential for high-efficiency solar cells. Here we report on Zn-rich ZnSnN₂ (Zn/Zn+Sn=0.67) photoluminescence, high-resolution X-ray diffraction, and electronic structure calculations based on Monte-Carlo structural models. The mutual compensation of Zn excess and O incorporation affords a desirable reduction of the otherwise degenerate n-type doping, but also leads to a strongly off-stoichiometric and disordered atomic structure. It is therefore remarkable that we observe only near-edge photoluminescence from well-resolved excitons and shallow donors and

acceptors. Based on first principles calculations, this result is explained by the mutual passivation of Zn_{Sn} and O_{N} defects that renders both electronically benign. The calculated bandgaps range between 1.4 and 1.8 eV, depending on the degree of non-equilibrium disorder. The experimentally determined value of 1.5 eV in post-deposition annealed samples falls within this interval, indicating that further bandgap engineering by disorder control should be feasible via appropriate annealing protocols.

1 Introduction

Development of new semiconducting materials has experienced a renaissance over the past decade, as prediction and screening capabilities for thin film inorganic compounds have reached new levels of sophistication. This activity has sparked interest in novel material classes, including the hybrid perovskites,¹ semiconducting ferroelectrics,² and spintronic materials.³ Another class of materials recently receiving attention is II-IV- V_2 semiconductors, which are structural analogs of the well-known III-V materials. ZnSnN_2 , part of the II-IV- V_2 class and analog to InN , is one such emergent material currently under investigation as a possible photovoltaic (PV) absorber.^{4,5}

It was originally predicted that the bandgap of ZnSnN_2 (ZTN) in its cation-ordered form would be near 2 eV, and that fully random cation ordering would result in a bandgap of 1 eV.⁶ However, later computational work showed that completely random cation occupation in ZTN would be a prohibitively high-energy structure to form.⁷ An alternative description of cation disorder in ZTN was proposed, which takes into account thermodynamic restrictions on the possible bonding configurations of the nitrogen atom.⁷ It was found that for ZTN material grown at thermal equilibrium, the octet-rule for the anion could be locally conserved while forming long-range disorder from alternating stacks of lattice planes with either $+120^\circ$ or -120° rotations. In this equilibrium disorder case, the bandgap was not found to vary significantly with degree of disorder. Another model for cation disorder in ZTN was developed from the perspective of non-equilibrium growth, in which octet-rule violations could be kinetically frozen in by growth methods such as sputtering.⁸ In this model, it was shown that the presence of octet-rule violating tetrahedra (e.g. $\text{Zn}_3\text{Sn}_1\text{-N}$ as opposed to the ground state $\text{Zn}_2\text{Sn}_2\text{-N}$) caused the bandgap to narrow, and that increasing the concentration of these off-stoichiometric “motifs” could cause the bandgap to

close entirely at fully-random cation occupation. It was also proposed that such “3:1-disorder” could be thermodynamically minimized with annealing, suggesting a possible way to control non-equilibrium cation disorder in ZTN.⁸

Unfortunately, the degenerate nature of stoichiometric ZTN has largely frustrated efforts to study the relationship between cation ordering and bandgap in this material.^{9,10} The problem is similar to the situation in early research on InN, the low bandgap member of the III-N materials, in which the fundamental gap was overestimated by >1 eV for decades due to a Burstein-Moss shift caused by degenerate n-type doping.¹¹ Despite these difficulties, effective methods for controlling the carrier density in ZTN have recently been developed, specifically by growing zinc-rich films with added hydrogen and then annealing in activated nitrogen.¹² However, the question of whether or not off-stoichiometric films with high defect density will have good carrier transport properties as a solar absorber remains unanswered.

In this work, we present an investigation into the structure, electronic quality, and defect interactions in low carrier density, zinc-rich ZTN. Using Pawley fitting of high-resolution X-ray diffraction, Monte Carlo simulated structures, and Rutherford backscattering spectrometry we determine that zinc-rich composition in ZTN is facilitated by the presence of oxygen by modeling the material as an alloy between ZnSnN_2 and ZnO . Zinc-rich films were found to exhibit only near-edge photoluminescence emission from excitons and shallow donors and acceptors, which attests to the high electronic quality of the material despite off-stoichiometry and structural disorder. This finding is explained using defect formation energy calculations that reveal mutual compensation between Zn_{Sn} and O_{N} defects, producing electronically benign defect complexes and reducing the density of charged defects. Together, these findings show that it is possible to achieve both low carrier density and high electronic quality in off-stoichiometric zinc tin nitride, which differentiates it from other emerging photovoltaic absorbers for which structural disorder precludes excellent electronic properties.

2 Methods

2.1 Experiment

Combinatorial Sputter Deposition. Four compositionally graded sample libraries of $\text{Zn}_{1+x}\text{Sn}_{1-x}\text{N}_2$ with $0 \leq x \leq 0.4$ were deposited by radio frequency (RF) co-sputtering onto stationary Eagle XG[®] glass

substrates heated to 200°C. In all four depositions, metallic zinc and tin targets inclined at 45° to the substrate normal were used as cation sources, and an RF plasma source positioned orthogonally to the substrate was used to supply activated forming gas. The forming gas mixture was 5% H₂ balanced in N₂. Two of the libraries were left as-deposited for characterization, while two of the libraries were annealed at 400°C for 6 h *in-situ* (i.e. without breaking vacuum) under pure reactive nitrogen flow and then allowed to naturally cool. Two libraries were deposited for each treatment type to ensure reproducibility of the results. The base pressure of the chamber immediately prior to each deposition was 10⁻⁶ Torr or less, as determined by an ion gauge. One additional library grown in pure nitrogen and left as-deposited, but otherwise grown using the same conditions as those described above, was used for comparison during the high-resolution X-ray diffraction measurements.

Characterization. Each sample was first characterized for cation composition and film thickness using spatially-resolved X-ray fluorescence spectroscopy (XRF). XRF was performed with Rh L-series excitation in energy-dispersive mode using Fischer XDV-SDD software, and a thickness model calibrated by DekTak profilometry. Throughout this work, the composition of each film is given as a ratio of the cation composition, Zn/(Zn+Sn), due to the inability of XRF to reliably measure nitrogen content. For reference, Zn/(Zn+Sn)=0.50 corresponds to stoichiometric composition (i.e. Zn₁Sn₁N₂ or 50% Zn on the cation sub-lattice) and any value larger than 0.50 corresponds to zinc-rich cation composition. Carrier density was measured as a function of zinc content using room temperature Hall effect measurements, as described in a previous work.¹² Regions of each library with cation composition Zn/(Zn+Sn) = 0.67, all of which exhibited n-type carrier density in the range 4 x 10¹⁶–2 x 10¹⁷ cm⁻³, were selected for photoluminescence (PL) spectroscopy. PL emission spectra were measured on 2-3 such regions from each library at 4.25 K using excitation with a 632.8 nm HeNe continuous wave laser operated at 10 mW, where the excitation spot diameter was approximately 250 μm. Variable temperature and power-dependent PL measurements were performed using the same excitation source. Excitation power spanned 0.1–10 mW at 4.25 K for the power-dependent measurements, and measurement temperature spanned 4.25–250 K at 10 mW for the temperature-dependent measurements. Finally high-resolution X-ray diffraction (HRXRD) measurements were taken as a function of zinc content for one annealed and one as-deposited sample library. Measurements were performed at the Stanford Synchrotron Radiation Lightsource (SSRL) beamline 2-1 using an X-ray energy of 15.5 keV (λ=0.7999 Å) and a Si(111) analyzer

crystal and photomultiplier tube detector. The diffraction patterns were collected in flat-plate geometry with an incident angle fixed at 2° to optimize the signal from the thin film and minimize the substrate background. Due to strong texturing in the deposited films, unit cell parameters were extracted via Pawley refinement of the HRXRD data using the TOPAS 6 Academic software package. We utilized the hexagonal Wurtzite prototype, space group $P6_3mc$, as the base structure for Pawley refinement. The data was well fit by standard Gaussian + Lorentzian peak broadening profiles with an anisotropic broadening factor to account for texturing.

2.2 Computation

First principles calculations were performed with the Vienna Ab initio Simulation Package (VASP) using the projector-augmented-wave (PAW) potentials.¹³ We employed density functional theory (DFT) in the generalized gradient approximation,¹⁴ on-site Coulomb interactions (DFT+U) for Zn-d orbitals ($U = 6$ eV),¹⁵ hybrid functionals,¹⁶ and total-energy calculations in the random-phase approximation (RPA).¹⁷ N and O soft pseudopotentials were used with a cut-off energy of 380 eV for the plane wave basis set. The ordered ground state of ZTN has an orthorhombic crystal structure in the space group $Pna2_1$ (33).

For defect calculations, a $2 \times 2 \times 2$ supercell with 128 atoms was constructed. The bulk/defect supercells were relaxed with a $2 \times 2 \times 2$ Gamma k-point mesh. The convergence criteria is when the total energy difference for each electronic step is less than 10^{-5} eV and total force on each ion is less than 0.02 eV. Defect formation energies with band gap corrections were performed as described in Ref. [18], where the GW corrected band gap value ($E_g = 1.41$ eV) was used (<https://materials.nrel.gov>). Finite size corrections were applied as described in Ref. [19]. For electronic structure calculations in disordered ZTN, we used the same supercells as for the defect calculations, and extended the approach of Ref. [8] for the case of off-stoichiometric (Zn-rich and O-containing) ZTN, which was achieved by including both N- and O-centered motifs in the model Hamiltonian. Monte-Carlo simulations and single-shot hybrid functional (SSH+U) calculations for the electronic structure were performed in an analogous fashion as in Ref. [8]. The mixing parameter (α) for the SSH+U functional was tuned to be 0.1617 for ZTNO supercells with $Zn/(Zn+Sn) = 0.67$. This choice can reproduce the GW calculated band structures of

small ZTNO cells with the same Zn or O ratio. A detailed account of the defect phase diagram in the Zn-Sn-N-O system and the resulting electronic structures will be given elsewhere.

3 Results and Discussion

3.1 Structure

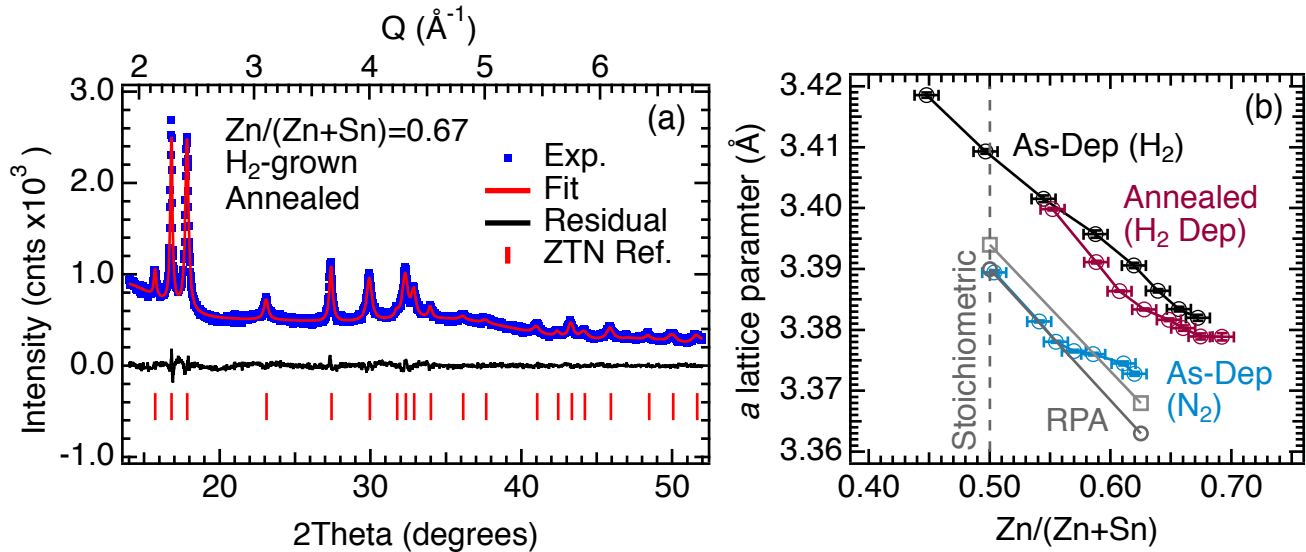


Figure 1: (a) Representative HRXRD diffraction pattern taken at 15.5 keV of an annealed ZTN film grown with added hydrogen (blue trace), and the associated Pawley fit (red trace) with residual (black trace). The red tick marks give the peak positions for cation-disordered, wurtzite ZTN. (b) Extracted a lattice parameter as a function of increasing zinc content for three sample libraries measured by HRXRD. The gray symbols in panel (b) give RPA-corrected a lattice parameters calculated from atomic models generated from MC simulations for $T_{\text{eff}} = 2000$ K (squares) and 700 K (circles) (more details in the text). The dashed vertical line indicates stoichiometric cation composition. For all films, a was found to decrease linearly with increasing zinc content up to a threshold. Note that the slope of the linear region of the experimental lines matches the slope of the computed lines, indicating good agreement between theory and experiment.

We begin by presenting HRXRD patterns for as-deposited and annealed ZTN films, grown either with added hydrogen or without, measured as a function of zinc content (Figure 1). Figure 1a shows representative HRXRD taken of a zinc-rich ($\text{Zn}/(\text{Zn}+\text{Sn})=0.67$), low carrier density sample of ZTN grown with added H_2 and annealed post-growth under activated nitrogen (blue trace).¹⁰ This sample corresponds to the champion low carrier density samples reported in a previous work.¹² The red trace is the associated Pawley fit, the black trace shows the residual between the fit and experiment, and the red tick marks give the peak positions for cation disordered, wurtzite ZTN (determined by processing a DFT-relaxed

structure through VESTA). An amorphous background can be seen in Figure 1a, which is an artifact of the glass substrates on which these films were grown, and has been discussed in more detail in a previous work.⁸ For SEM imaging of the microstructure for as-deposited and annealed films, we direct the reader to the supplemental information of Ref. [12].

A peak shift to higher diffraction angle was observed with increasing off-stoichiometry for all peaks in the three measured libraries (as-deposited, as-deposited with added H₂, and grown with H₂ then annealed). Diffraction patterns for the three ZTN libraries were fit using Pawley refinement to extract the *a*-parameter as a function of zinc content, as shown in Figure 1b. The value of the *a*-parameter was found to decrease linearly with increasing zinc content up to a threshold for the three sample libraries. After the threshold in zinc content, the variation in *a*-parameter with zinc content deviates from linearity, although the value of *a* continues to decrease. Note that for the samples grown in hydrogen (maroon and black symbols), the *a*-parameter is offset to larger values compared to the values for the N₂-grown library across the entire zinc composition range. This offset can be explained as resulting from hydrogen incorporation in the lattice, which is supported by the lower hydrogen content measured by secondary ion mass spectrometry (SIMS) in N₂-grown films compared to H₂-grown films reported in a previous work.¹²

Generally, XRD peak shifts like those observed in Figure 1b can be thought of in the context of Vegard's Law, in which linear lattice parameter shifts for an alloy of two materials (A and B) indicate successful A_{1-x}B_x mixing on a single crystal lattice without phase separation.^{21,22} For the zinc-rich ZTN films in this work, which are known to contain approximately 14 at.% oxygen (see Figure S1 in the Supplemental), the most plausible alloy model would be between stoichiometric ZnSnN₂ and ZnO, since both materials share a wurtzite crystal structure (as opposed to the binary Zn₃N₂ phase, which has anti-bixbyite structure).²³ For such an alloy to form, oxygen impurities would need to incorporate onto lattice sites, specifically as oxygen substitutional defects (O_N), which have been proposed several times previously.^{4,12,24} Thus, we hypothesize that low carrier density, zinc-rich ZTN grown in the presence of background oxygen consists of an alloy between ZnSnN₂ and ZnO, in which carrier density is reduced via the formation of defect complexes involving oxygen and excess zinc.

Based on this alloy hypothesis, we performed Monte-Carlo (MC) simulations for off-stoichiometric Zn_{1+x}Sn_{1-x}(N_{1-x}O_x)₂. The temperature in the MC calculations can be identified with the "effective temperature" (T_{eff}) that is used as a descriptor for non-equilibrium growth.²⁵ Thus, as-grown films

with a higher degree of non-equilibrium disorder have a higher T_{eff} that can be far above the actual growth temperature. During annealing, the disorder is reduced and T_{eff} approaches the actual anneal temperature. We use here $T_{\text{eff}} = 2000$ K as an estimate for the as-grown film,²⁵ and $T_{\text{eff}} = 700$ K for the limit of a more-equilibrated annealed film. In order to correct the systematic overestimation of lattice parameters in DFT-GGA by 1–2%, we determined a scaling factor obtained from random phase approximation (RPA) calculations for the Pmc2₁ structure of ZTN, which has a smaller 8-atom primitive cell.⁷ Thus, for the ordered Pna2₁ ground state of ZTN, we obtained $a = 6.773$ Å, $b = 5.879$ Å, and $c = 5.509$ Å. These orthorhombic a and b values correspond to an average hexagonal lattice constant of $a = 3.390$ Å. The atomistic models of the MC simulations were used to determine the composition dependence of the lattice constants, which is discussed further below.

Notably, the calculated wurtzite lattice constant agrees perfectly with the experimental value for stoichiometric ZTN deposited without H₂ (blue symbols), although an uncertainty around 0.01 Å (0.3%) should be expected even after the RPA correction.²⁶ More importantly, the rate of decrease of the calculated a -parameters with increasing zinc content is in excellent agreement with that of the experimentally-determined values. This consistency with experiment allows two conclusions to be drawn: (1) excess zinc in off-stoichiometric films occupies cation sites instead of forming a secondary phase, and (2) oxygen incorporation encourages formation of the zinc-rich structure, which supports the ZnSnN₂/ZnO alloy hypothesis proposed above.

3.2 Photoluminescence Spectroscopy

Next we present photoluminescence (PL) emission spectra taken at 4.25 K for zinc-rich, annealed ZTN films grown in hydrogen (Figure 2; the same films as the zinc-rich films in Figure 1). Three films displayed in Figure 2 were as-deposited and three were annealed under activated nitrogen. For each set (red and grey), two spectra were measured on different regions of the same thin film library, and the third spectrum was measured for a second library. For all films, a broad PL emission peak is observed near 1.42 eV, but the intensity and line shapes vary depending on the sample. For annealed films (red traces), a sharper peak appears near 1.48–1.50 eV. As described below, this high-energy peak is assigned to bound excitons in the higher-electronic-quality annealed films.

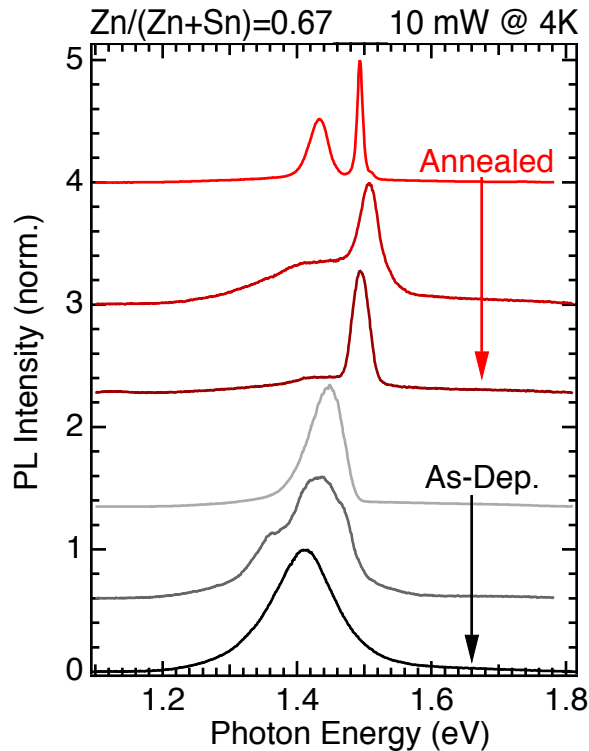


Figure 2: Representative low-temperature PL spectra from ZTN samples with $\text{Zn}/(\text{Zn}+\text{Sn})=0.67$, either annealed or as-deposited, plotted with a vertical offset and normalized for comparison. All spectra were taken from samples with n-type carrier density in the range 4×10^{16} – $2 \times 10^{17} \text{ cm}^{-3}$. Note the appearance of a peak at 1.48–1.50 eV for films that have been annealed, and the absence of such a peak for as-deposited films.

Literature reports on ZTN photoluminescence are consistent with the PL data shown here. Previously, we observed luminescence in the range 1.35–1.50 eV for as-deposited films with varying stoichiometry (all zinc-rich).⁴ Two works by another group reported PL emission spectra for ZTN grown by the vapor-liquid-solid method (VLS), in which transitions at 1.50 eV and 1.72 eV were ascribed to defect and near-band-edge luminescence, respectively.^{7,27} Given that the films were grown closer to equilibrium than the films in this work (VLS growth being similar to flux growth), the higher energy luminescence may be the result of a wider bandgap due to a lower fraction of non-equilibrium disorder.

Attribution of the PL emission in Figure 2 to exciton (annealed samples) and band-edge (as-deposited samples) recombination are supported by the lineshapes, temperature and power-dependencies (see below), and by comparison with the room temperature optical absorption spectra shown for annealed and as-deposited films in Figure S2 of the Supplemental.

To identify the origin of PL emission peaks in Figure 2, we used power- and temperature-dependent PL measurements. As shown in Figure 3a, the 1.49 eV peak position does not shift with increasing laser power, while the peaks centered around 1.42 eV blue-shift by 25 meV/decade of excitation (black

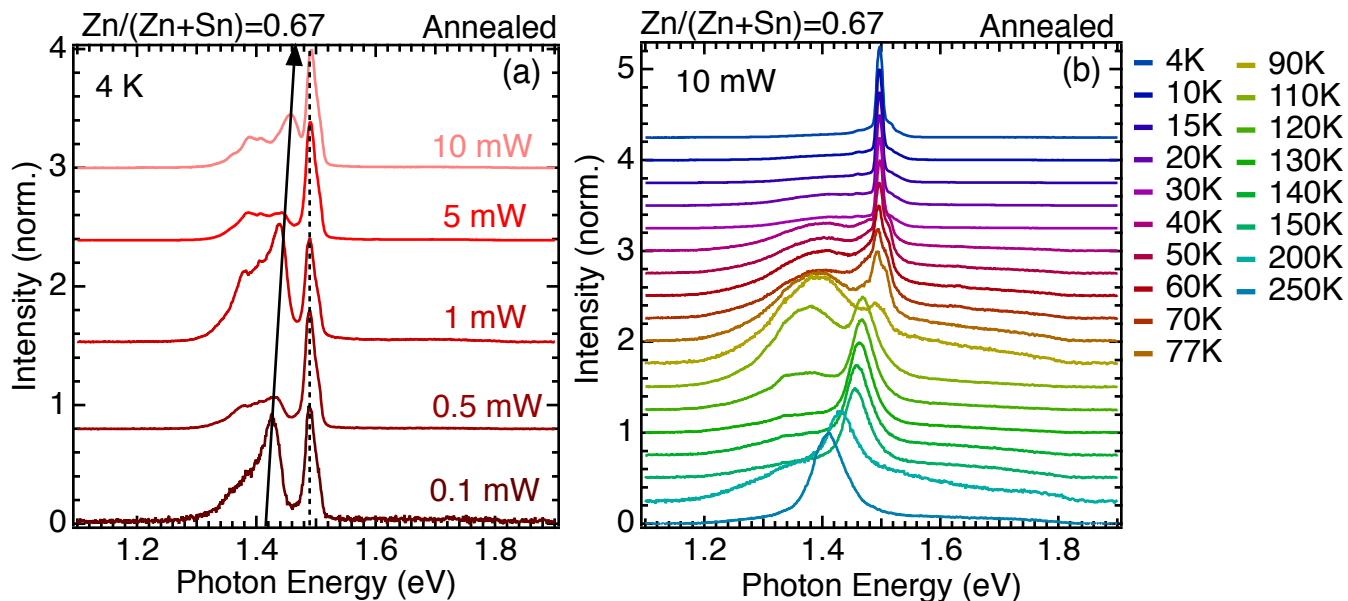


Figure 3: Power dependent (a) and temperature-dependent (b) PL emission spectra taken of the same annealed, zinc-rich sample with $\text{Zn}/(\text{Zn}+\text{Sn})=0.67$. Spectra in both panels are vertically offset for ease of comparison. In panel (a), the peak at 1.49 eV does not shift as laser power is increased. Several peaks are observed at lower energy, and these blue-shift with increasing laser power. In panel (b), the 1.49 eV peak intensity is quenched as measurement temperature increases. Emission above 90 K is attributed to band-edge luminescence.

arrow). In addition, the linewidth for 1.49 eV emission is constant when injection changes by 100x, while the sub-band structure of the low-energy peak changes significantly. As shown in Figure S3 of the Supplemental, the PL emission intensity vs. excitation intensity data can be described as power laws $PL \propto P^n$, where $n = 1.1$ for the exciton emission and $n = 0.88$ for the defect emission. The exponent $n < 1$ is typical for defect emission, while $n > 1$ is typical for exciton emission.²⁸

As a function of temperature (Figure 3b), the 1.49 eV peak intensity decreases until quenching after 90 K (yellow trace). This suggests that the thermal energy at >100 K is larger than the exciton binding energy, and emission at higher temperatures is attributed to the free and bound carriers, not excitons. A semiconductor with a bandgap of 1.5 eV is expected to have approximate exciton binding energy of 7-8 meV (e.g., GaAs or InP), and free carrier emission at >100 K is typical for such semiconductors. As expected, the free/bound carrier PL emission peak ($T >100$ K) is broader than the exciton PL emission peak ($T <100$ K).

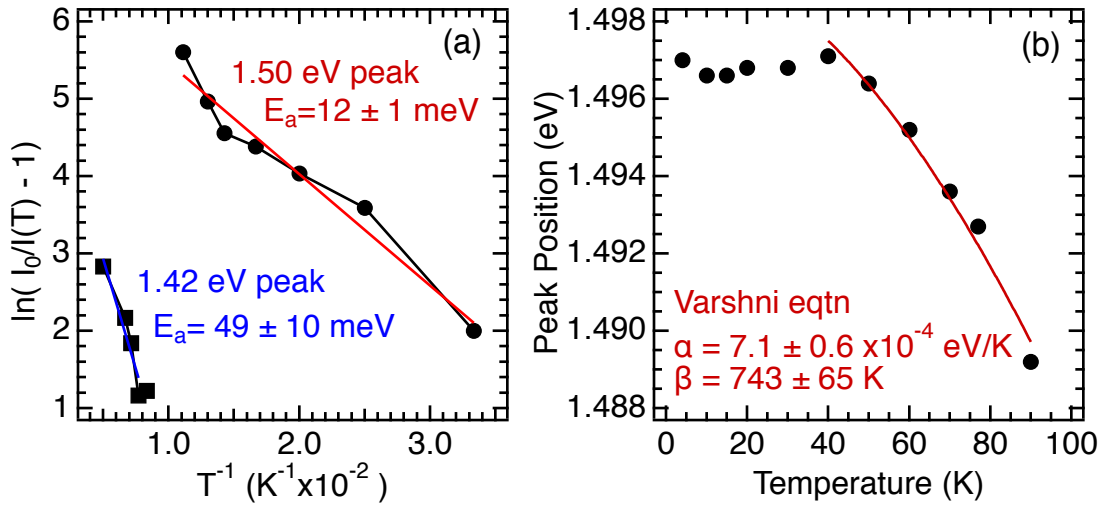


Figure 4: (a) Arrhenius analysis of the intensity of the 1.49 eV (red line, circles) and 1.42 eV (blue line, squares) peaks as a function of temperature (more details in the text). For the 1.49 eV and 1.42 eV peaks, activation energies of 12 ± 1 meV and 49 ± 10 meV were found, respectively. (b) Shift of the 1.49 eV peak as a function of temperature. The data has been fit with the Varshni equation, which yielded a temperature dependence of the direct bandgap $E_g(T) = 2 \times 10^{-4}$ eV/K.

We used the model of Equation (1) to analyze the temperature-dependent intensity of the exciton and defect PL emission:

$$I(T) = \frac{I_0}{(1 + Ae^{-E_a/k_B T})} \quad (1)$$

where I_0 is the PL peak intensity at 0 K, A is a constant, k_B is Boltzmann's constant, and E_a is the activation energy for the transition.²⁸ We find $E_a^{defect} = 49 \pm 10$ meV for the 1.42 eV peak, and $E_a^{exciton} = 12 \pm 1$ meV for the 1.49 eV peak. $E_a^{exciton} = 12 \pm 1$ meV is slightly larger than the expected free exciton binding energy (≤ 10 meV), and could indicate the exciton binding energy to defects. Because the defect (1.42 eV) PL emission band has complex structure, only a limited temperature range was used in estimating the defect activation energy. Defect PL emission is discussed in detail in Section 3.3.

In addition, the high-energy PL peak shift in Figure 3b is indicative of temperature-dependent bandgap changes. Therefore, we used the Varshni equation to analyze the bandgap temperature dependence.²⁹

$$E_g(T) = E_g(0) - \frac{\alpha T^2}{T + \beta} \quad (2)$$

This analysis is shown in Figure 4b, where we find $E_g(0) = 1.497$ eV. The Varshni parameters extracted for the zinc-rich, annealed ZTN film used in Figures 3 and 4 are $\alpha = 0.71 \pm 0.06$ meV/K and $\beta = 488 \pm 40$ K. These values lie intermediate to the values for GaN ($\alpha, \beta = 0.91$ meV/K, 830 K)³⁰ and InN

(0.41 meV/K, 454 K).³¹ The temperature dependence of the bandgap for zinc-rich ZTN was determined to be 0.2 meV/K, or ~ 60 meV over the range 0–300 K.

3.3 Defect Luminescence

As observed in Figure 3a, the defect PL peak (1.42 eV) blue-shifts by 25 meV/decade of excitation. In semiconductors dominated by point defects, a PL peak that shifts to higher energy with increased laser power is attributed to donor-acceptor pair (DAP) recombination, in which the blue-shift occurs due to increasing stabilization of donor-acceptor pairs by their Coulomb attraction in the final state.^{32–35} However, for heavily doped or highly compensated semiconductors, the DAP model does not apply, because it assumes the concentration of point defects (or dopants) to be dilute.^{34,36} For the films in this work, which are best modeled as an alloy between ZnSnN_2 and ZnO due to zinc-rich composition and significant oxygen incorporation, any dilute-defect assumption could be erroneous. Therefore, the 1.42 eV PL peak observed for the films in this work cannot be explained using the DAP model.

Two other possibilities for the origin of the 1.42 eV peak are electrostatic potential fluctuations at the band edges,^{34,37–39} or variations in the bandgap due to varying degrees of cation disorder after annealing.^{8,40} In the potential fluctuations model (sometimes termed quasi-donor-acceptor-pair),^{38,40} spatial variation in the distribution of defects throughout the semiconductor leads to variation in the extent of the defect states into the bandgap.³⁷ In the bandgap variation model, non-uniform distribution of ordered and disordered cation arrangements causes the band edge densities of states to fluctuate.⁴⁰ In both cases, the blue-shift with increased laser power results from photogenerated carriers filling local energy minima, which causes additional carriers generated by increased excitation to populate the available higher energy states. Also in both cases, the red-shift with increasing temperature is caused by increased carrier mobility allowing carriers trapped in local minima to overcome the potential barriers and redistribute to lower-energy levels. Either of these models would be a good fit for the origin of the 1.42 eV peak observed in this work.

3.4 Defects and Electronic Structure

At this point, it is important to discuss how exciton emission can be observed, considering these films are known to have high point defect density and significant atomic and structural disorder. We note

that the exciton peak is only observed for *annealed* ZTN films, suggesting the annealing treatment modifies the electronic structure such that exciton emission is enhanced. To understand how this might occur, we used calculated defect formation energies coupled with bandgap calculations for $\text{ZnSn}(\text{N}_{1-x}\text{O}_x)_2$ (ZTNO) to compare the effects of defect interactions and thermal equilibration to the conclusions drawn in Section 3.4. These data are presented in Figure 5.

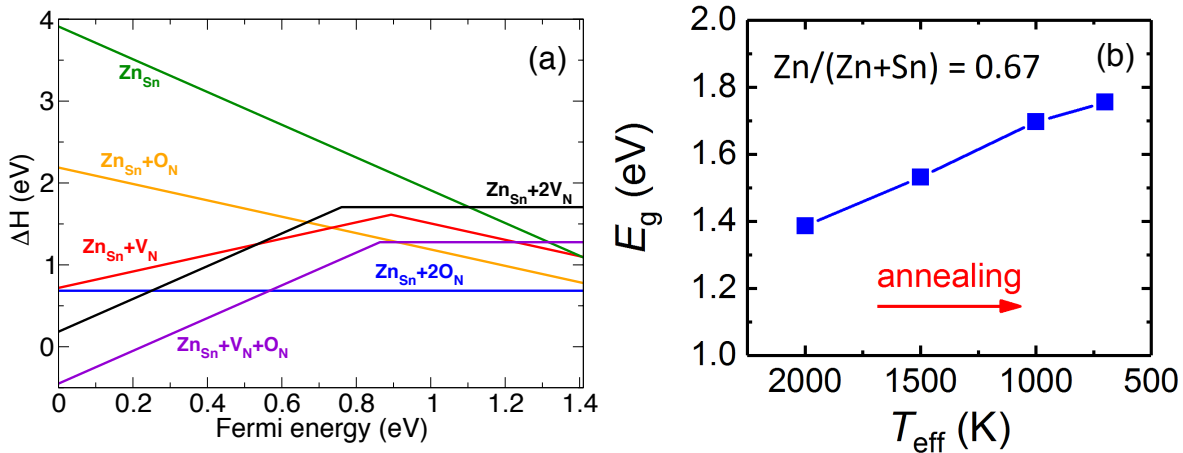


Figure 5: (a) Defect formation energies calculated for the isolated Zn_{Sn} acceptor and different possible defect complexes involving Zn_{Sn} . Details on the chemical potentials and bandgap used are given in the text. Note the significant reduction in formation energy for the Zn_{Sn} acceptor when complexed with a pair of O_{N} donors. (b) The band gap calculated in the SSH+U approach as a function of the effective temperature T_{eff} in the Monte Carlo simulation for $\text{Zn}/(\text{Zn}+\text{Sn}) = 0.67$. The bandgap determined from the PL data is consistent with $T_{\text{eff}} = 1500$ K, indicating an intermediate level of thermal equilibration.

Our defect calculations show a strong preference for oxygen incorporation in ZTN, and that oxygen presence plays an essential role in compensating Zn excess. Figure 5a shows the defect formation energy (ΔH_f) as a function of Fermi energy for the isolated Zn_{Sn} defect and a number of possible defect complexes involving Zn_{Sn} . These calculations were performed using nitrogen chemical potential $\Delta\mu_{\text{N}} = +0.50$ eV, Zn chemical potential $\Delta\mu_{\text{Zn}} = -0.52$ eV, and oxygen chemical potential $\Delta\mu_{\text{O}} = -3.22$ eV. The positive non-equilibrium value for $\Delta\mu_{\text{N}}$ was used to account for the activated nitrogen source utilized in deposition,⁴¹ $\Delta\mu_{\text{Zn}}$ was taken at the phase boundary between ZTN and Zn_3N_2 to account for zinc-rich composition, and $\Delta\mu_{\text{O}}$ was taken at the equilibrium with ZnO. As seen in Figure 5a, the formation energy of the Zn_{Sn} acceptor for n-type ZTN (i.e. $\Delta E_F \approx E_{\text{CBM}}$) decreases sequentially as it complexes with an increasing number of O_{N} donors (going from green, to yellow, to blue lines). Such low formation energy of the $\text{Zn}_{\text{Sn}}+2\text{O}_{\text{N}}$ complex is consistent with the significant oxygen incorporation measured by RBS (Figure S1), and explains the ability to grow highly Zn-rich films in this and previous works without

precipitation of Zn_3N_2 or ZnO secondary phases.^{4,12} Furthermore, the mutual compensation of Zn_{Sn} and O_{N} supports the $\text{ZnSnN}_2/\text{ZnO}$ alloy hypothesis proposed earlier.

Figure 5b shows the calculated bandgap of ZTNO as a function of the effective temperature (T_{eff}) defined in Section 3.1 for the Monte Carlo (MC) simulations. The calculated bandgaps were obtained from two independent MC seeds at the same composition ($\text{Zn}/(\text{Zn}+\text{Sn}) = 0.67$) as the samples used for PL analysis. We find the ZTNO bandgap widens as T_{eff} decreases in the MC simulation, which corresponds to decreasing non-equilibrium disorder (i.e. minimizing the fraction of $\text{N-Zn}_3\text{Sn}_1$ tetrahedra).⁸ During cooling in the MC runs, short range order was found to increase, indicated by larger fractions of energetically preferable $\text{N-Zn}_2\text{Sn}_2$ and O-Zn_4 motifs. Compared to previous MC simulations in stoichiometric ZnSnN_2 ,⁸ the excess Zn/O incorporation in these models leads to a larger bandgap for comparable T_{eff} . The reduction of T_{eff} in the MC simulations in this work can be correlated with the experimental annealing treatment. Thus, the 1.5 eV bandgap estimated from the PL measurements corresponds to $T_{\text{eff}} \approx 1500$ K, which is consistent with annealed films having a lower degree of non-equilibrium disorder, and suggests that suitable annealing protocols could lead to a further increase in the bandgap.

Taken together, the conclusions from the defect and bandgap calculations can be used to understand how exciton luminescence is observed in the films in this work. We note that the lowest formation energy complex in Figure 5a ($\text{Zn}_{\text{Sn}}+2\text{O}_{\text{N}}$) is a neutral defect pair, which renders it electronically benign. Upon annealing, the ZTN films discussed herein are brought closer to equilibrium (as shown in Figure 5b), which encourages formation of the benign $\text{Zn}_{\text{Sn}}+2\text{O}_{\text{N}}$ defect. Thus, there is reason to believe that annealing treatment reduces the density of defect states in the bandgap by forming these neutral complexes, resulting in higher electronic quality and allowing exciton luminescence to be observed despite structural disorder. Indeed, the beneficial effect of removing defect levels and scattering centers by forming charge-neutral complexes has been observed in other materials systems, e.g. in CuInSe_2 ⁴² and MgZnO .⁴³ Finding evidence for this effect in zinc tin nitride suggests that appropriate growth and annealing protocols can be used to produce material with both low carrier density and good minority carrier transport properties.

4 Conclusion

Here we have presented an experimental and computational investigation into the structure, electronic quality, and defect interactions in low carrier density, zinc-rich ZTN. We observed near band edge photoluminescence from well-resolved excitons and shallow defects in zinc-rich material with a high degree of structural disorder. First principles calculations explain this result by the mutual passivation of Zn_{Sn} and O_{N} defects that forms electronically benign defect complexes and reduces the density of charged defects in the material. Calculated bandgaps for $\text{ZnSn}(\text{N}_{1-x}\text{O}_x)_2$ as a function of effective temperature showed the bandgap widens as non-equilibrium disorder decreases, which can be correlated to the effects of the annealing treatment in experiment. The bandgap estimated from PL data for low carrier density material is 1.5 eV, corresponding to an intermediate level of disorder and suggesting that bandgap tuning through disorder control should be possible via appropriate annealing protocols. Ultimately, the results of this work demonstrate the possibility to achieve high electronic quality in off-stoichiometric zinc tin nitride despite structural disorder, which places it in company with other successful thin film PV materials.

5 Conflicts of Interest

There are no conflicts of interest to declare.

6 Acknowledgements

This material is based upon work supported by the U.S. Department of Energy's (DOE) Office of Energy Efficiency and Renewable Energy (EERE) under Solar Energy Technologies Office (SETO) Agreement Number 30302. This work used computational resources sponsored by EERE, located at the National Renewable Energy Laboratory (NREL). Use of the Stanford Synchrotron Radiation Light-source, SLAC National Accelerator Laboratory, is supported by DOE's Office of Science (SC), Basic Energy Sciences (BES) under Contract No. DE-AC02-76SF00515. X-ray diffraction measurements at SLAC were also supported by DOE-SC-BES, Materials Sciences and Engineering Division.

References

- [1] W.-J. Yin, J.-H. Yang, J. Kang, Y. Yan and S.-H. Wei, *Journal of Materials Chemistry A*, 2015, **3**, 8926–8942.
- [2] Z. Fan, K. Sun and J. Wang, *Journal of Materials Chemistry A*, 2015, **3**, 18809–18828.
- [3] M. C. Prestgard, G. P. Siegel and A. Tiwari, *Advanced Materials Letters*, 2014, **5**, 242–247.
- [4] A. N. Fioretti, A. Zakutayev, H. Moutinho, C. Melamed, J. D. Perkins, A. G. Norman, M. Al-Jassim, E. S. Toberer and A. C. Tamboli, *Journal of Materials Chemistry C*, 2015, **3**, 11017–11028.
- [5] K. Javaid, J. Yu, W. Wu, J. Wang, H. Zhang, J. Gao, F. Zhuge, L. Liang and H. Cao, *physica status solidi (RRL) - Rapid Research Letters*, 2017, 1700332.
- [6] N. Feldberg, J. D. Aldous, W. M. Linhart, L. J. Phillips, K. Durose, P. A. Stampe, R. J. Kennedy, D. O. Scanlon, G. Vardar, R. L. F. III, T. Y. Jen, R. S. Goldman, T. D. Veal and S. M. Durbin, *Applied Physics Letters*, 2013, **103**, 042109.
- [7] P. C. Quayle, E. W. Blanton, A. Punya, G. T. Junno, K. He, L. Han, H. Zhao, J. Shan, W. R. L. Lambrecht and K. Kash, *Phys. Rev. B*, 2015, **91**, 205207.
- [8] S. Lany, A. N. Fioretti, P. P. Zawadzki, L. T. Schelhas, E. S. Toberer, A. Zakutayev and A. C. Tamboli, *Physical Review Materials*, 2017, **1**, 035401.
- [9] L. Lahourcade, N. C. Coronel, K. T. Delaney, S. K. Shukla, N. A. Spaldin and H. A. Atwater, *Advanced Materials*, 2013, **25**, 2562–2566.
- [10] A. N. Fioretti, E. S. Toberer, A. Zakutayev and A. C. Tamboli, *42nd IEEE Photovoltaic Specialist Conference (PVSC)*, 2015, 1–5.
- [11] W. Walukiewicz, J. W. Ager III, K. M. Yu, Z. Liliental-Weber, J. Wu, S. X. Li, R. E. Jones and J. D. Denlinger, *Journal of Physics D: Applied Physics*, 2006, **39**, R83.
- [12] A. N. Fioretti, A. Stokes, M. R. Young, B. Gorman, E. S. Toberer, A. C. Tamboli and A. Zakutayev, *Advanced Electronic Materials*, 2017, **3**, 1600544.
- [13] G. Kresse and D. Joubert, *Physical Review B*, 1999, **59**, 1758–1775.

- [14] J. P. Perdew, K. Burke and M. Ernzerhof, *Physical Review Letters*, 1996, **77**, 3865–3868.
- [15] S. L. Dudarev, G. A. Botton, S. Y. Savrasov, C. J. Humphreys and A. P. Sutton, *Physical Review B*, 1998, **57**, 1505–1509.
- [16] J. Heyd, G. E. Scuseria and M. Ernzerhof, *The Journal of Chemical Physics*, 2006, **124**, 219906.
- [17] J. Harl and G. Kresse, *Physical Review B*, 2008, **77**, 045136.
- [18] H. Peng, D. O. Scanlon, V. Stevanovic, J. Vidal, G. W. Watson and S. Lany, *Physical Review B*, 2013, **88**, 115201.
- [19] S. Lany and A. Zunger, *Modelling and Simulation in Materials Science and Engineering*, 2009, **17**, 084002.
- [20] J. Pan, *Unpublished*.
- [21] L. Vegard, *Zeitschrift für Physik*, 1921, **5**, 17–26.
- [22] A. R. Denton and N. W. Ashcroft, *Physical Review A*, 1991, **43**, 3161–3164.
- [23] D. E. Partin, D. J. Williams and M. O’Keeffe, *Journal of Solid State Chemistry*, 1997, **132**, 56–59.
- [24] S. Chen, P. Narang, H. A. Atwater and L.-W. Wang, *Advanced Materials*, 2014, **26**, 311–315.
- [25] P. F. Ndione, Y. Shi, V. Stevanovic, S. Lany, A. Zakutayev, P. A. Parilla, J. D. Perkins, J. J. Berry, D. S. Ginley and M. F. Toney, *Advanced Functional Materials*, 2014, **24**, 610–618.
- [26] H. Peng and S. Lany, *Physical Review B*, 2013, **87**, 174113.
- [27] P. C. Quayle, K. He, J. Shan and K. Kash, *MRS Communications*, 2013, **3**, 135–138.
- [28] I. Pelant and J. Valenta, *Luminescence spectroscopy of semiconductors*, Oxford Univ. Press, Oxford, 2012.
- [29] Y. P. Varshni, *Physica*, 1967, **34**, 149–154.
- [30] I. Vurgaftman, J. R. Meyer and L. R. Ram-Mohan, *Journal of Applied Physics*, 2001, **89**, 5815–5875.

- [31] J. Wu, W. Walukiewicz, W. Shan, K. M. Yu, J. W. Ager III, S. X. Li, E. E. Haller, H. Lu and W. J. Schaff, *Journal of Applied Physics*, 2003, **94**, 4457–4460.
- [32] P. Y. Yu and M. Cardona, *Fundamentals of Semiconductors: Physics and Materials Properties*, Springer, New York, 2010.
- [33] D. Kuciauskas, P. Dippo, A. Kanevce, Z. Zhao, L. Cheng, A. Los, M. Gloeckler and W. K. Metzger, *Applied Physics Letters*, 2015, **107**, 243906.
- [34] I. Dirnstorfer, M. Wagner, D. M. Hofmann, M. D. Lampert, F. Karg and B. K. Meyer, *physica status solidi (a)*, 1998, **168**, 163–175.
- [35] P. W. Yu, *Journal of Applied Physics*, 1977, **48**, 5043–5051.
- [36] M. Wagner, I. Dirnstorfer, D. M. Hofmann, M. D. Lampert, F. Karg and B. K. Meyer, *physica status solidi (a)*, 1998, **167**, 131–142.
- [37] B. I. Shklovskii and A. L. Efros, *Electronic properties of doped semiconductors*, Springer Science & Business Media, New York, 1984.
- [38] T. Gershon, B. Shin, N. Bojarczuk, T. Gokmen, S. Lu and S. Guha, *Journal of Applied Physics*, 2013, **114**, 154905.
- [39] S. A. Jensen, S. Glynn, A. Kanevce, P. Dippo, J. V. Li, D. H. Levi and D. Kuciauskas, *Journal of Applied Physics*, 2016, **120**, 063106.
- [40] G. Rey, G. Larramona, S. Bourdais, C. Choné, B. Delatouche, A. Jacob, G. Dennler and S. Siebentritt, *Solar Energy Materials and Solar Cells*, 2018, **179**, 142–151.
- [41] C. M. Caskey, R. M. Richards, D. S. Ginley and A. Zakutayev, *Materials Horizons*, 2014, **1**, 424–430.
- [42] S. B. Zhang, S.-H. Wei, A. Zunger and H. Katayama-Yoshida, *Physical Review B*, 1998, **57**, 9642–9656.
- [43] Y. Ke, S. Lany, J. J. Berry, J. D. Perkins, P. A. Parilla, A. Zakutayev, T. Ohno, R. O’Hayre and D. S. Ginley, *Advanced Functional Materials*, 2014, **24**, 2875–2882.